Time Accurate Unsteady Pressure Loads Simulated for the Space Launch System at a Wind Tunnel Condition

Stephen J. Alter*, Gregory J. Brauckmann†, Bil Kleb‡,
Craig L. Streett§, Christopher E. Glass*, David M. Schuster¶
NASA Langley Research Center
Hampton, Virginia 23681-2199

Using the Fully Unstructured Three-Dimensional (FUN3D) computational fluid dynamics code, an unsteady, time-accurate flowfield about a Space Launch System configuration was simulated at a transonic wind tunnel condition (Mach = 0.9). Delayed detached eddy simulation combined with Reynolds Averaged Naiver-Stokes and a Spallart-Almaras turbulence model were employed for the simulation. Second order accurate time evolution scheme was used to simulate the flowfield, with a minimum of 0.2 seconds of simulated time to as much as 1.4 seconds. Data was collected at 480 pressure taps at locations, 139 of which matched a 3% wind tunnel model, tested in the Transonic Dynamic Tunnel (TDT) facility at NASA Langley Research Center. Comparisons between computation and experiment showed agreement within 5% in terms of location for peak RMS levels, and 20% for frequency and magnitude of power spectral densities. Grid resolution and time step sensitivity studies were performed to identify methods for improved accuracy comparisons to wind tunnel data. With limited computational resources, accurate trends for reduced vibratory loads on the vehicle were observed. Exploratory methods such as determining minimized computed errors based on CFL number and sub-iterations, as well as evaluating frequency content of the unsteady pressures and evaluation of oscillatory shock structures were used in this study to enhance computational efficiency and solution accuracy. These techniques enabled development of a set of best practices, for the evaluation of future flight vehicle designs in terms of vibratory loads.

Nomenclature

a	speed of sound
aam	aft attachment component on -Z side of booster
aap	aft attachment component on +Z side of booster
b	booster component
CFL	Courrant, Fredricks, Lewey number
D_{ref}	reference diameter
f	frequency, Hz
fa	forward attachment component on booster
hc	core component
hs	entire stack
M	Mach number
P	pressure
$Turb$	turbulence measure
u, v, w	velocity components

*Aerospace Research Engineer, Aerothermodynamics Branch; Senior Member AIAA
†Aerospace Research Engineer, Aerothermodynamics Branch; Associate Fellow AIAA
‡Assistant Branch Head, Computational Aerosciences Branch; Senior Member AIAA
§Senior Aerospace Engineer, Computational Aerosciences Branch
¶Senior Research Engineer, NASA Engineering Safety Center, Associate Fellow AIAA

X	X-coordinate, axially nose to tail
Y	Y-coordinate, pitch axis where boosters oppose
Z	Z-coordinate
α	angle of attack, degrees
β	side slip angle, degrees
γ	ratio of specific heats
Δt'	non-dimensional time step
ρ	density

Subscripts

R	residual
Rm	mean flow residual
Rt	temporal residual

Introduction

The next generation of heavy lift launch vehicles NASA is developing is the Space Launch System (SLS). The SLS is being designed to enable access to low Earth orbit, the international space station (ISS), and exploration of other celestial bodies. To reduce the development costs for this vehicle, which is needed given the budgetary complexities of the United States government,[1] previously developed hardware from the Constellation program is being used to build initial configuration.

The initial configuration of the SLS is a merged design of the Ares I and Ares V vehicles,[2] and termed Block 1. As the SLS design evolves,[3] as shown in Figure 1, several changes are to be made to ensure this vehicle has the capacity to lift at least 130 metric tons of cargo. The Block 1 version of the SLS is designed to lift 105 metric tons. The configuration is comprised of two boosters attached to a central main rocket powered with five Space Shuttle main engines (SSME). Each of the SLS boosters has four Space Shuttle Orbiter solid rocket booster (SRB) segments instead of the original 3 segments that were used for a single SRB of the Space Shuttle Orbiter.

Of the many development challenges facing the SLS, buffet is being investigated in the transonic regime of ascent. Buffet is characterized by a frequency on the order of 1 to 20 Hz caused by the unsteady pressure environment with a vibratory loading that can cause issues with the structural integrity of a flying vehicle. Computational fluid dynamics (CFD) has yet to be proven a viable alternative to wind tunnel testing in developing buffet forcing functions for structural analyses. CFD shortcomings for computing unsteady surface pressure environments, that can lead to determination of buffet forcing functions, are usually exposed in the requirements to obtain accurate predictions on a time scale and resolution, necessary to capture low frequency loads. Low frequency loads are usually on the order of 3Hz to 100Hz, where the buffet frequencies are a subset. However, as will be shown in later sections, to keep solutions accurate, time steps are on the order of 1.0×10^{-6} to 2.0×10^{-6} second. Thus, long run times on dense meshes with FUN3D is needed to get to the frequency spectrum of an unsteady surface pressure environment.

This report discusses the progress in FUN3D to predict the unsteady flow environments for transonic flight vehicles, towards the eventual development of buffet forcing functions. An unstructured mesh flow solver is used to compute such an environment on an SLS configuration. Since wind tunnel test data exists for comparison of results, accuracy of flow solutions can be assessed for needed requirements to do such computations. Mesh resolution and time step studies are performed to determine the best practices for the intended goal. Sections on the flow solver and mesh generation methods, computational resources and techniques, post processing data and baseline configuration results are presented. The data developed for this study was used to develop frequency and power spectral density, to evaluate the unsteady flowfield compared to wind tunnel test data. Utilizing the practices identified in this report, can improve successful filtering of design changes, to reduce adverse frequencies based loading of flight vehicles and lead to the development of computationally based buffet forcing functions.

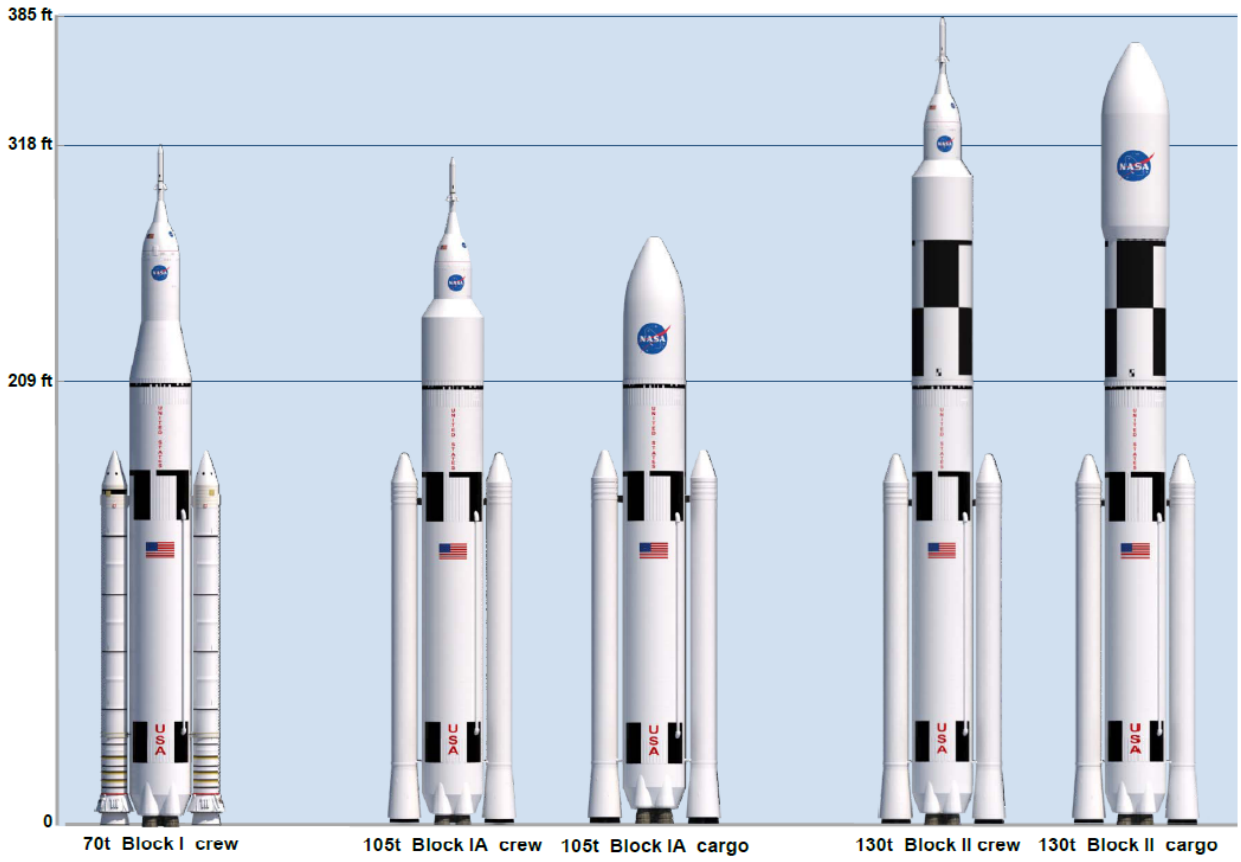

Figure 1. SLS variants.

Geometric Model

Computations performed for the SLS stack used the Block 1A cargo configuration, shown in Figure 2. The Block 1A configuration was reduced in complexity by removing fasteners such as bolts, surface stiffening ribs and fuel feed lines to make a smooth outer mold line. This shape is referred to as a simplified rigid buffet model (RBM). The orientation of this model for computational work has the X-coordinate extending down the body from the nose towards the base. The Z-coordinate is tangential to the pitch plane (α), so that the booster is in the X-Y plane. The Y-coordinate extends from the mid-body symmetry located between both boosters, extending towards a booster.

The origin of the vehicle is at the nose tip, however for clarity of the shape, the axis shown in Figure 2 is offset. Angle of attack is set when the body is rotated in the X-Z plane about the Y-axis, and side slip is located in the X-Y plane when the vehicle is rotated about the Z-axis. For the computations, initially a quarter body was considered where part of the booster and central rocket, or core, was used. With only a quarter of the vehicle, a rapid succession of computations was possible to gain experience with respect to grid point distributions. However, when a half body was used, the flow on the core under the booster was predicted to be asymmetric, as shown in Figure 3. Thus, the computations that were used for this study were predominantly half body, with an X-Z plane of symmetry, with a few full body configurations to ensure accurate capture of all physical properties of the flow domain.

Different booster nose shapes were used to study their effect on the unsteady loads. These nose shapes include the five additional noses to the baseline shown in Figure 4. Each nose geometry was simply swapped into the computer aided design (CAD) model prior to generating the computational meshes.

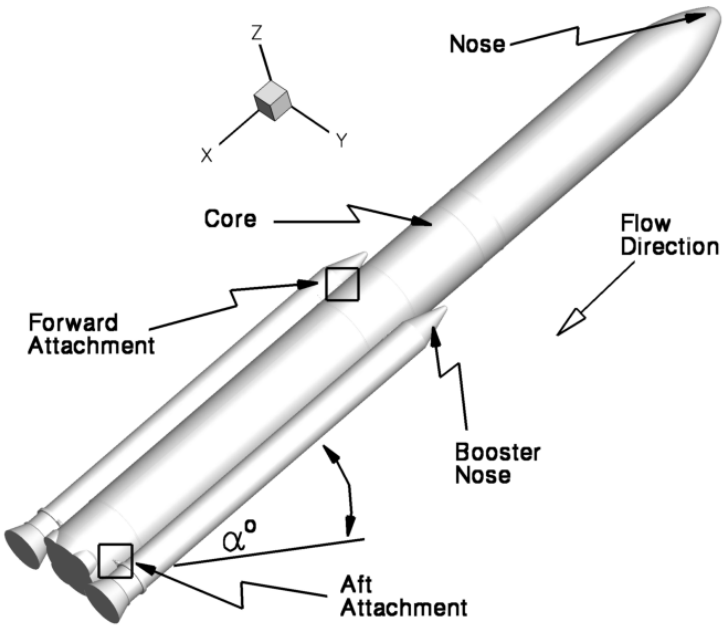

Figure 2. Baseline SLS stack with coordinate system used for computations.

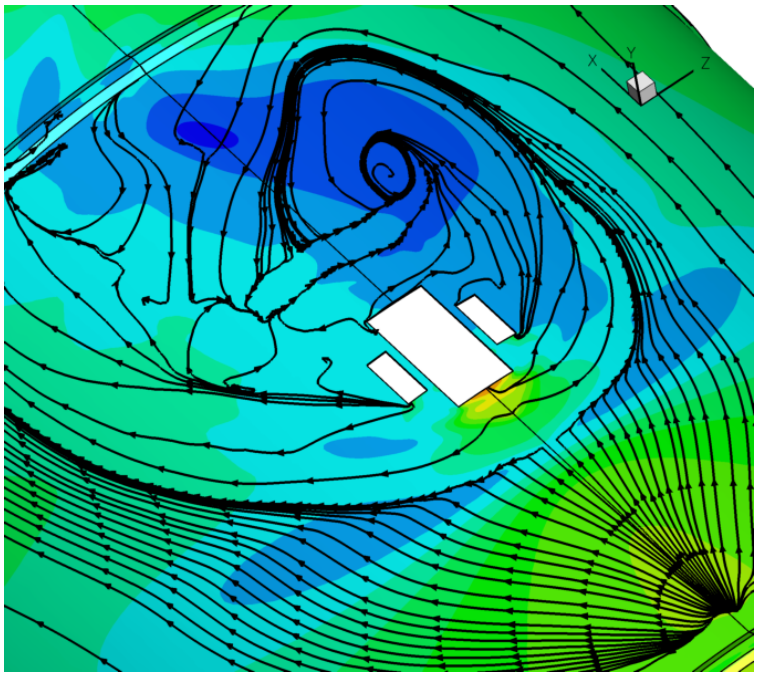

Figure 3. SLS core contoured with pressure illustrating asymmetric flowfield.

Mesh Generation Method

Generation of the surface and volume meshes for this study was done using the NX[4] CAD tool, GridEx,[5,6] and AFLR3.[7,8] The NX CAD tool was used to generate all solid manifold representations of geometry used in the course of this work. The original data used as input for the grid generation process either originated from NX itself by using the parametric modeling features or by loading in CAD parts from other sources for the SLS geometries. An example of the NX interface with the simplified RBM geometry displayed is shown

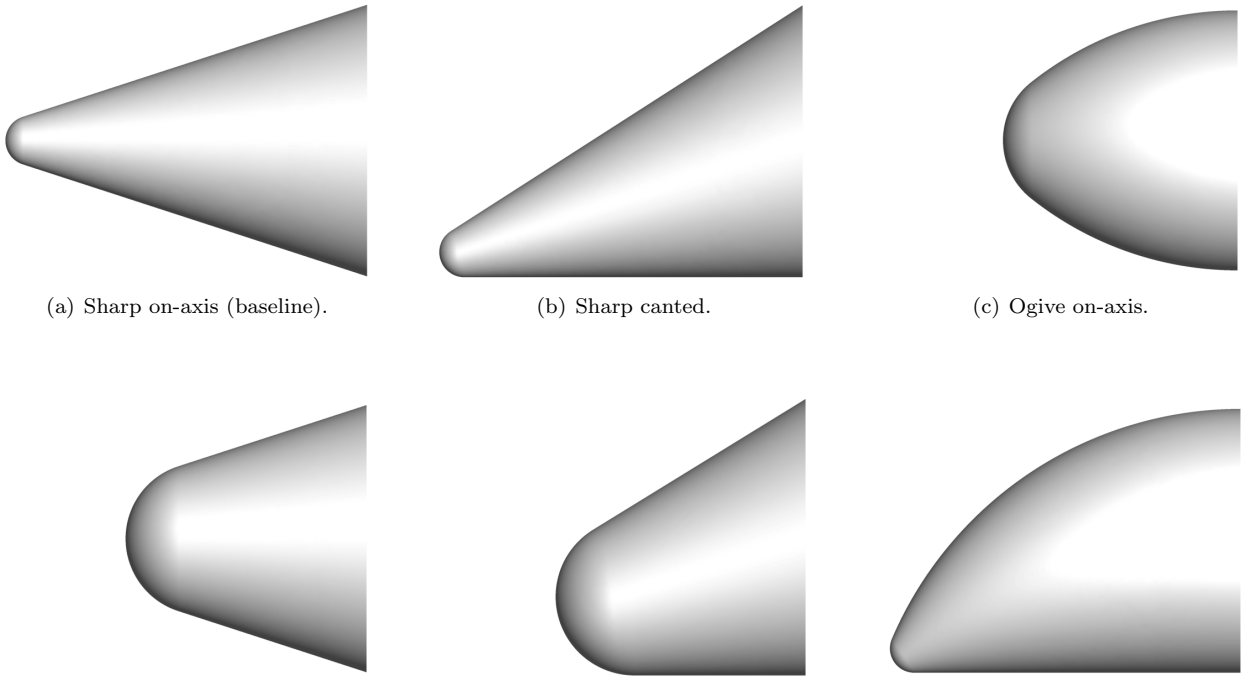

(a) Sharp on-axis (baseline). (b) Sharp canted. (c) Ogive on-axis.

(d) Blunt on-axis. (e) Blunt canted. (f) Ogive canted.

Figure 4. Booster nose shapes (viewed parallel to pitch plane).

in Figure 5.

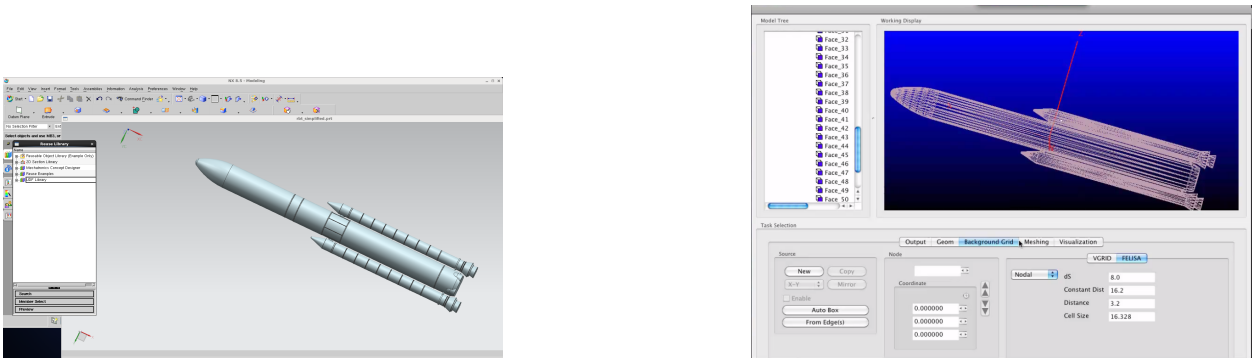

(a) NX. (b) GridEx.

Figure 5. RBM simplified model displayed in the NX CAD and GridEx software.

When completed in NX, a parasolid part file was written for use with GridEx. GridEx is a graphical front end that enables the user to develop input data for the AFLR3 unstructured grid generator, and use the FELISA[9,10] or VGRID[11,12] mesh generators to develop surface grids used by AFLR3. It utilizes the same geometry kernel that NX uses for solid model construction through an application interface (API) with CaPRi.[13] This API enables grids to be generated on the actual CAD description of models using the native CAD geometry engine that created the data, thereby eliminating data loss as would be encountered if using IGES or STEP model descriptions. As shown in Figure 5, the GridEx software enables a user to define and set controlling parameters for the mesh generation process. For the meshes used in this study, a reference cell size was used for the determination of all other cell size specifications in the mesh model. This enables the re-sizing of the mesh based on a single parameter for subsequent mesh resolutions to be used, including those developed for a mesh sensitivity study discussed in a following section.

The end result of running GridEx is a batch script that can be used with BatchEx, the GridEx command-line driven software for generating the input data sets to AFLR3. After running the AFLR3 software, an unstructured volume mesh results. Shown in Figure 6, is a surface mesh for a typical geometry.

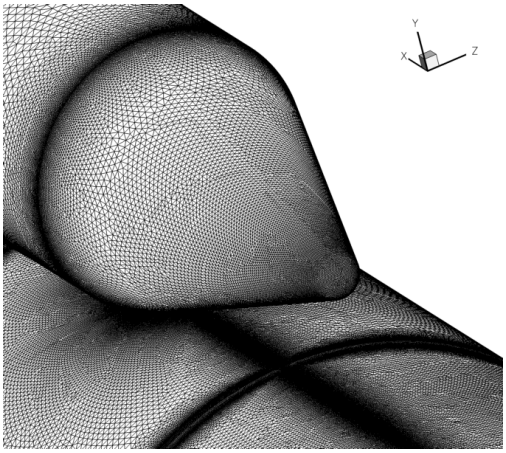

Figure 6. Baseline unstructured surface mesh from AFLR3.

Flow Solver and Approach

Computational analyses of the unsteady flowfield for the SLS Stack were performed using the Fully UNstructued Three-Dimensional (FUN3D) software.[14] For these computations, FUN3D was used to solve the unsteady Reynolds-Averaged Navier-Stokes (RANS) equations on a node-based, mixed element mesh, for compressible flow. A selectively dissipative version of the Low-Dissipation Flux Splitting Scheme (LDFSS) inviscid flux function[15] and a modified[16] Van Albada limiter[17] were used throughout the domain. A modified Delayed-Detached Eddy Simulation (DDES) turbulence model was used with a Spallart-Allmaras[18] (SA) model.

To facilitate efficient computing, both time step and mesh density sensitivities were evaluated based on convergence criteria. The generic procedure used to determine convergence was to establish a target frequency, where the solution remained accurate with respect to fast Fourier transforms of unsteady pressure data, at points along the SLS stack, to find a consistent power spectral density compared to wind tunnel data.

For FUN3D, the non-dimensional time step used for this study was defined by Equation 1. This non-dimensional time step equates to the range of time steps mentioned previously.

$$\Delta t' = \frac{a_\infty}{200 f D_{ref}} \tag{1}$$

In this equation, f is the highest frequency of interest in Hz which is 60Hz for the 3% model scale, 200 represents the number of discrete time steps per cycle, α_∞ is the freestream speed of sound, and D_{ref} is the core diameter reference length.

While unsteady flow solutions can be started with a steady state solution, the solutions for the current study were begun as unsteady from the start of the computation. To aid in rapid reduction of transients, the flowfield was initialized with quiescent flow conditions and then the solution was computed at a $\Delta t'$ of 0.1 for 2,500 steps, then 0.01 for another 2,500 steps, and finally 0.003 for the remainder of the computation. This application of different non-dimensional time steps provided the necessary removal of start-up transients in the solution, thereby enabling the basic flowfield structures to set up quickly. As shown in Figure 7, applying the final non-dimensional time step commensurate with more accurate computing, enabled capture of the unsteady surface pressures after 5,000 computed time steps. Sudden changes in frequency at 2500 and 5000 time steps indicates a switch to a smaller time step.

Shown in Figure 8a, sudden drops in residual magnitude are indicative of changes in the non-dimensional time steps. Spikes in the residuals when computing at the final non-dimensional time step are merely local divergence of the linear solver inside FUN3D and posed no serious affect on the computations. Approximately

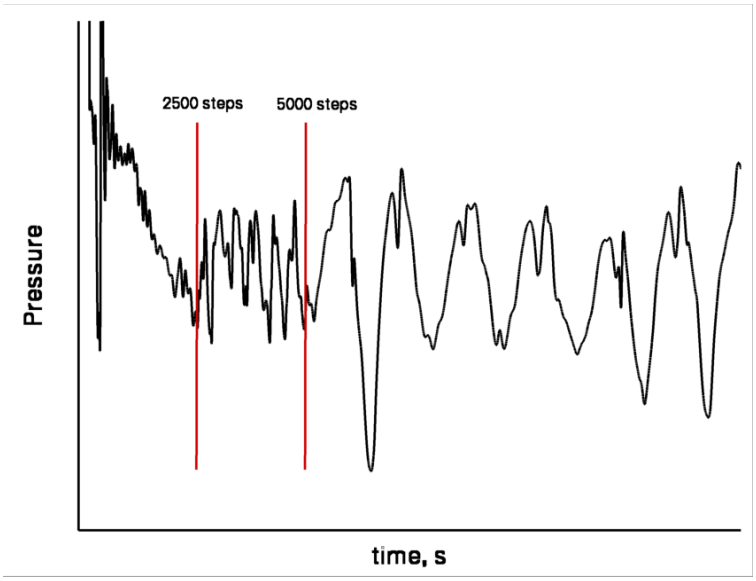

Figure 7. Unsteady surface pressure signature near the forward attachment for the initial computing of a solution.

one tenth of the total time used to wash out the higher frequency errors with larger non-dimensional time steps, prior to reducing the low frequency errors, was sufficient before using the computed data for further analyses.

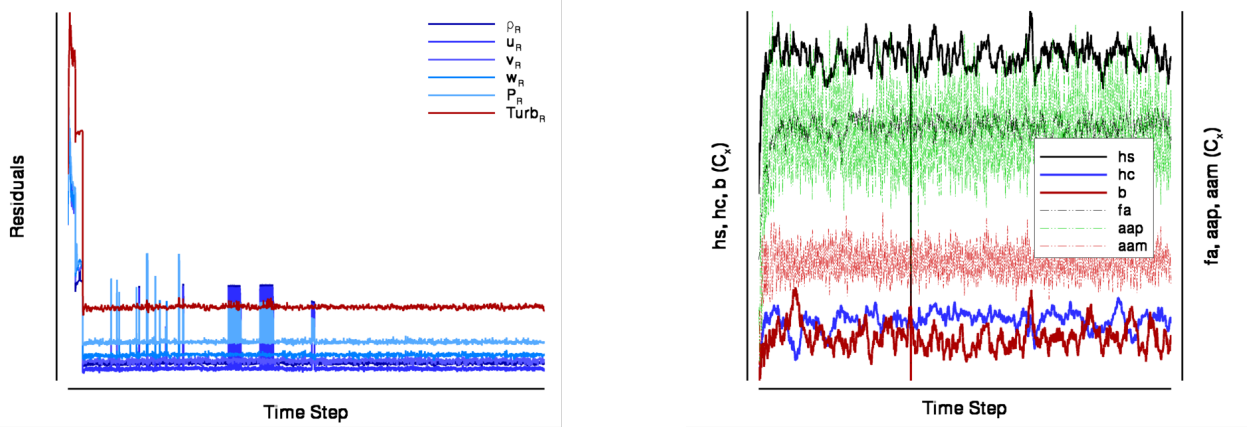

(a) Residual history.

(b) Force and moments.

Figure 8. Solver performance and body force and moments for a typical computation time of half a second.

Shown in Figure 8b are the forces and moments for a typical computation. This particular computation was for approximately half a second of time, requiring almost 10 days of computing on 2,500 Ivy Bridge cores, using the baseline mesh of nearly 35 million nodes. While the periodicity of the data is difficult to determine, all data was post processed with Fast Fourier transforms to determine both the frequency of the loading and the power of the frequencies.[19]

Other parameters used to control the accuracy of the solver include the number of steady-state sub-iterations between time steps. A rule-of-thumb when using FUN3D for determining the sub-iteration count, is that the mean flow residuals should be at least one order of magnitude less than the temporal residual error. Not obtaining this relationship could result in the truncation errors from the mean flow adversely affecting the quality of the solution. Unfortunately, due to the time step size, it was not possible to get the mean flow residuals lower than the residual temporal errors. However, as shown in Figure 9, several different

counts of sub-iteration were used to find the best compromise between mean flow to temporal residual errors. For most of the computations, a count of 7 sub-iterations were used. Subsequent sub-iteration count studies were performed, each for changes in mesh resolution and non-dimensional time step, to ensure the validity of the computations.

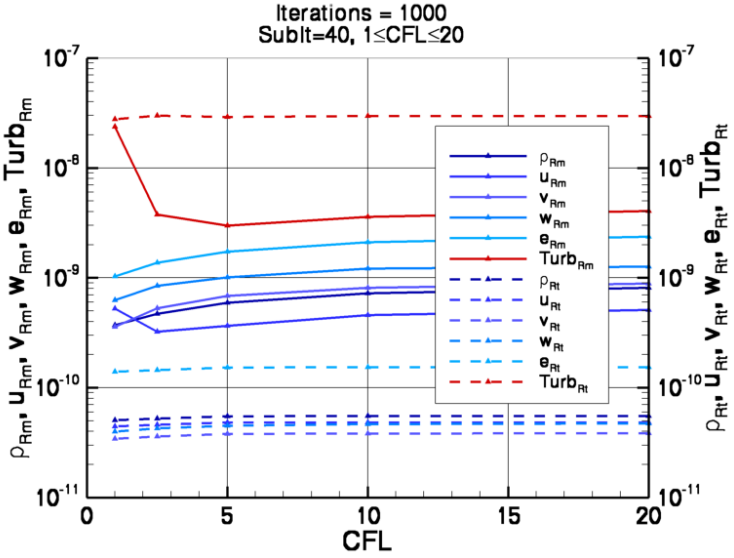

Figure 9. Mean flow and temporal error flowfield variables residual sensitivity to CFL.

Sensitivities

To accurately and efficiently compute the variety of cases needed for this study, sensitivity of time step and mesh size had to be determined. Most computations were performed at the NASA Advanced Supercomputing Facility where the Pleiades supercomputer resides. Pleiades has in excess of 165,000 cores, enabling usage of a multitude of cores to be used in a computation. However, FUN3D has a general requirement of no less than 12,500 nodes per computing core, without suffering from communications swamping the computations. Thus, there is a threshold of time required to obtain a solution. While it would be ideal to use the smallest time step and largest number of nodes that could fit onto Pleaides for highly accurate computations, such work could not be completed in a reasonable amount of calendar days. Thus, sensitivity analyses were performed to determine the best time step and mesh resolution to use, without adversely affecting accuracy or turnaround time.

Time Step Sensitivity

A time step sensitivity analysis was performed for the cases computed per Equation 1, in this study. Using the target frequency of 100Hz, a non-dimensional time step of 0.003 resulted. Increasing and decreasing this time step had significant impacts on the accuracy of the unsteady surface pressure environment. As shown in Figure 10a, increasing the non-dimensional time step produced a phase shift in the unsteady pressures, evidenced by the axial force coefficient (C_x) per simulation time elongating as simulation time increases. Decreasing the non-dimensional time step below 0.003 showed diminishing returns with improved accuracy. Although a slight change in phase is noted between the non-dimensional time steps of 0.002 and 0.003, computing at 0.003 is 50% faster than at 0.002.

Further investigation of the time sensitivity, using the unsteady surface pressure environment is shown in Figure 10b. In Figure 10b, the symbols represent computed frequency data, while the interpolated curve is an approximation through those points. To obtain this plot, more than 160,000 time steps were computed, but only a few points identified the general frequency were the unsteady pressures had the most impact on the configuration. Thus, the curve is too sparse to see without the interpolated curve.

A power spectral density analysis of the frequencies for different time steps, was performed. As can be

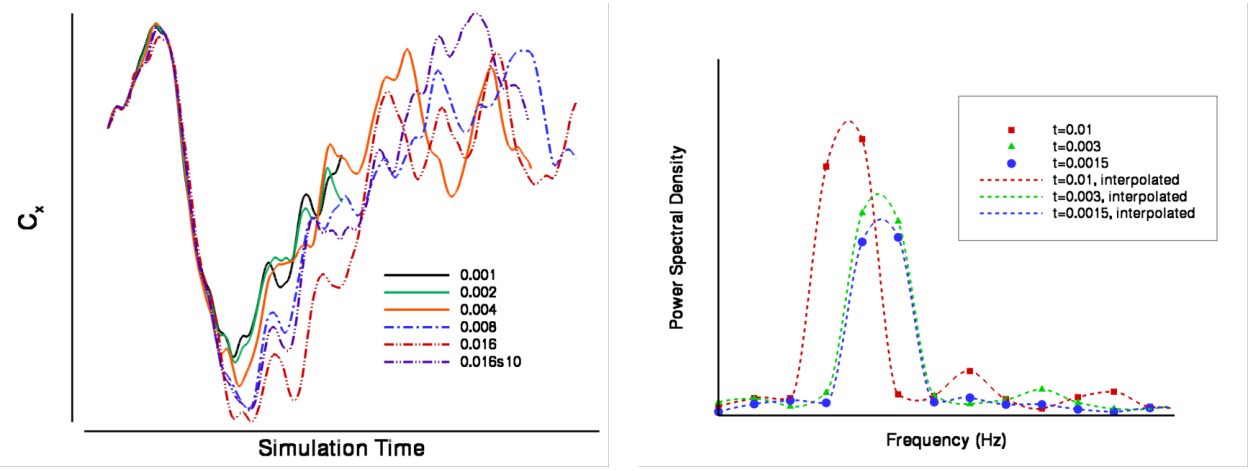

(a) Axial force.

(b) Power spectral density.

Figure 10. Frequency phase shift due to changing the non-dimensional time step.

seen in Figure 10b, as the time increases, frequency decreases, which is synonymous with the elongation of the axial force frequency in Figure 10a. As the non-dimensional time step is decreased, the differences diminish. While ever decreasing time steps are desirable, the smaller the time step, the longer a computation has to be performed, to accumulate sufficient data for analyses. Thus, for pragmatic reasons, a non-dimensional time step of 0.003 was used throughout this study.

Mesh Size Sensitivity

Another sensitivity evaluated for this computation was mesh density. To capture the boundary layer gradients accurately, approximately 50 prismatic cells extending orthogonally from the wall, were used. The grid density was significant for the remainder of the domain, due to sizing it to 10 times the body length in $\pm X$, +Y and $\pm Z$ computational directions. In the construction of these meshes, a single cell size was used to provide a characteristic length for the remainder of the mesh. Shown in Figure 11 are three different density meshes used in the characterization of the mesh sensitivity.

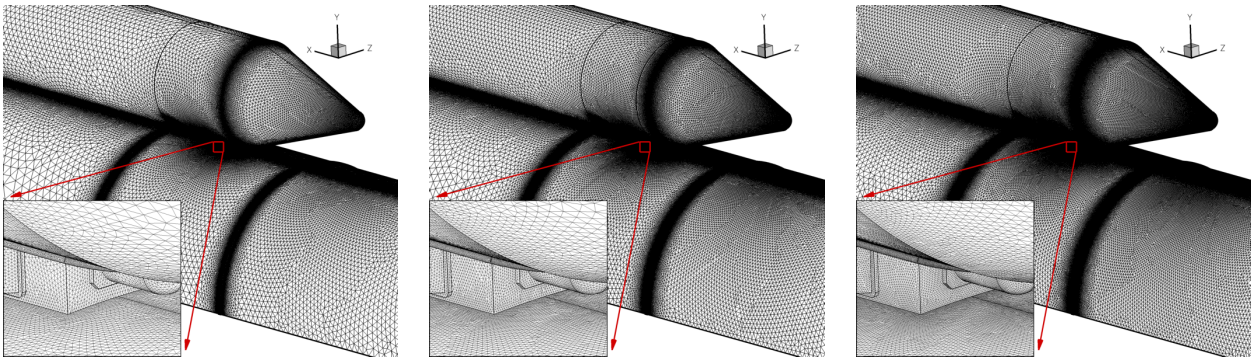

(a) Coarse (20M).

(b) Medium (35M).

(c) Fine (59M).

Figure 11. Mesh density variation for a sensitivity analyses, with the medium mesh as the baseline density and node count in parenthesis.

The baseline characteristic scale for the reference cell size on which all other sources are dependent, is defined to be a scale of 1. Sources for the mesh generation were scaled based on this characteristic length. By referencing the characteristic cell size for the remainder of the mesh and using this length to define all other sources, mesh size could be controlled by simply changing this single cell size by some factor. Increasing the scale produced fewer nodes in the mesh while reducing it produced increased node counts. Because the same sources for defining the mesh generation process were simply scaled by the characteristic scale, all generated

meshes are within family; they are related to one another in cell distribution, mesh density, and overall mesh quality. As noted in Figure 11, the coarse mesh is a scale of 1.3, whereas the fine mesh had a scale of 0.8. Using these meshes to compute the unsteady surface pressure fields, the mesh sensitivity is expressed in a power spectral density plot shown in Figure 12.

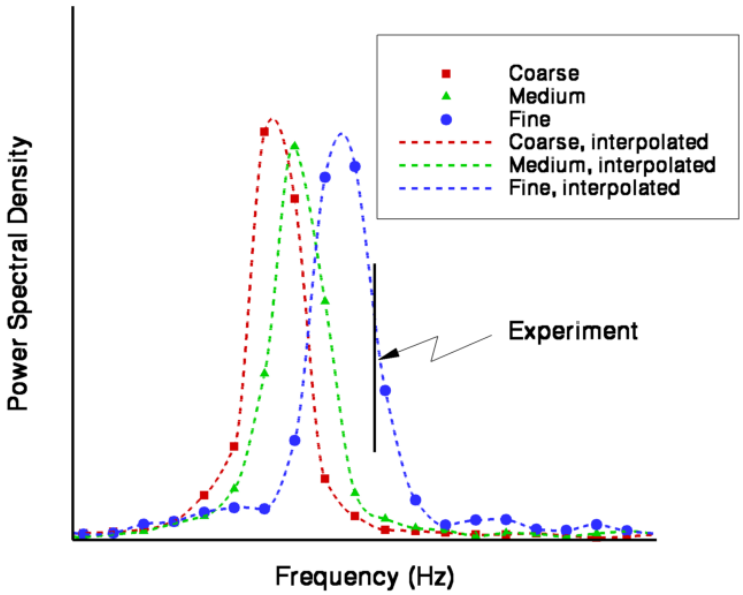

Figure 12. Solution accuracy based on a grid sensitivity analysis.

The data in Figure 12 has the same issue of being sparse as Figure 10, requiring the use of interpolated curves through the data, to get a sense of the shift in frequency as the mesh density changes. Shown in Figure 12, as the grid is refined, the peak PSD is closer to the experiment for the simplified RBM configuration computed. Although this study would suggest that increasing the grid resolution would improve agreement with experimental data, it would also result in a mesh density that would be impractical for multiple computations. The purpose of this study was to not get the experimental value exactly, but rather to use the computational analyses for filtering design changes. Thus, the baseline mesh size of 35 million nodes was deemed sufficient for the bulk of the computations.

Results and Post Processing

For the final paper, flowfield content will be described for the baseline configuration, with detailed explanations of how the extensive computed data was post processed into information for guiding the ongoing studies.

Acknowledgments

This work was done in support of the NASA Engineering Safety Center (NESC), for the Space Launch System Program. The authors which to acknowledge the guidance provided by John Blevins of NASA Marshal Space Flight Center, Russ Rausch of NASA Langley Research Center, and David Schuster of the NESC. CAD geometries, provided by NASA Marshal Space Flight Center, were modified to develop solid manifold bodies for use with the mesh generation software, by Scott Buynildsen of Vigyan and Ben Penatzer of ATI.

References

[1]Lyles, G., Flores, T., Hundley, J., Feldman, S., and Monk, T., "Complex Decision–Making Applications for the NASA Space Launch System," IEEEAC Paper 1278, M11–1229, IEEE, April 2012.

[2]Congress, U. S., "Utilization of Existing Workforce and Assets in Development of Space Launch System and Multi Purpose Crew Vehicle," *NASA Authorization Act of 2010*, Vol. S.3729, United States 111^{th} Congress, Washington, D. C., October 2010, p. 12.

[3]Pritchett, V. E., Mayle, M. N., Blevins, J. A., Crosby, W. A., and Purinton, D. C., "Aerodynamic Tests of the Space Launch System for Database Development," Tech. Rep. 2014–1256, AIAA, January 1992.

[4]"NX (Unigraphics) from Siemens PLM Software, Plano, TX," `http://www.plm.automation.siemens.com/en_us/products/nx`.

[5]Jones, W. T., "GridEx – An Integrated Grid Generation Package for CFD," AIAA Paper 2003–4129, 2003.

[6]Jones, W. T., "An Open Framework for Unstructured Grid Generation," AIAA Paper 2002–3192, 2002.

[7]Marcum, D. L. and Weatherill, N. P., "Unstructured grid generation using iterative point insertion and local reconnection," *AIAA Journal*, Vol. 33, No. 9, 1995, pp. 1619–1625.

[8]Marcum, D. L., "Efficient Generation of High-Quality Unstructured Surface and Volume Grids," *Engineering With Computers*, Vol. 17, No. 3, 2001, pp. 211–233.

[9]Peiro, J., Peraire, J., and Morgan, K., "FELISA Reference Manual and User's Guide, Volume I," University of Wales/Swansea Report CR/821/94, 1994.

[10]Perairee, J., Peiro, J., and Morgan, K., "Multigrid Solution of the 3D Compressible Euler Equations on Unstructured Tetrahedral Grids," *International Journal of Numerical Methods Engineering*, Vol. 36, No. 6, 1993, pp. 1029–1044.

[11]Parikh, P., Pirzadeh, S., and Löhner, R., "A Package for 3-D Unstructured Grid Generation, Finite-Element Flow Solutions, and Flow-Field Visualization," Contractor Report CR–182090, NASA, September 1990.

[12]Löhner, R. and Parikh, P., "Three-Dimensional Grid Generation by the Advancing Front Method," *International Journal of Numerical Methods and Fluids*, Vol. 8, 1988, pp. 1135–1149.

[13]Haimes, R. and Follen, G., "Computational Analysis Programming Interface," *Proceedings of the 6th International Conference on Numerical Grid Generation in Computational Field Simulation*, edited by Cross, Eiseman, Hauser, Soni, and Thompson, July 1998, pp. 10—20.

[14]Anderson, W. K., Gropp, W. D., Kaushik, D. K., Keyes, D. E., and Smith, B. F., "Achieving High Sustained Performance in an Unstructured CFD Application," NASA CR–2000–210080, National Aeronautics and Space Administration/ICASE, January 2000.

[15]Edwards, J. R., "A Low–Diffusion Flux–Splitting Scheme for Navier–Stokes Calculation," *Computers and Fluids*, edited by M. Deville, Vol. 26, Elsevier, July 1997, pp. 653–659.

[16]Vatsa, V. N. and White, J. A., "Calibration of a Unified Flux Limiter for Ares-Class Launch Vehicles from Subsonic to Supersonic Speeds," Jannaf paper, JANNAF, April 2009.

[17]van Albada, G. D., van Leer, B., and Roberts, W. W., "A comparative Study of Computational Methods in Cosmic Gas Dynamics," *Astronomy and Astrophysics*, edited by J. Lequeux and M. Grewing, Vol. 108, EDP Sciences, April 1982, pp. 76–84.

[18]Spalart, P. R. and Allmaras, S. R., "A One-Equation Turbulence Model for Aerodynamic Flows," AIAA Paper 92–0439, AIAA, January 1992.

[19]Brauckmann, G. J., Alter, S. J., Kleb, W. L., Glass, C. E., and Murphy, K. J., "Computational Predictions of Unsteady Pressures for an SLS Configuration With Modified Booster Nose Shapes and Comparison to Experiment," AIAA Paper 2015–(submitted), American Institute of Aeronautics and Astronautics, January 2015.